Filtered High Gain Observer for an Electric Vehicle's Electro-hydraulic Brake: Design and Optimization Using Multivariable Newton-based Extremum Seeking

Jamal El-bakkouri[1*], *Hamid Ouadi*[2], *Fouad Giri*[3] *and Mohamed Khafallah*[1]

(1. ENSEM, Hassan II University of Casablanca, Casablanca BP 8118, Morocco;
2. ENSAM Rabat, Mohammed V University, Rabat BP 6207, Morocco;
3. Department of Electrical Engineering, University of Caen Normandy, Caen 14032, France)

Abstract: Designing high-gain observers (HGOs) for the state estimation of an electric vehicle's electrohydraulic brake (EHB) system is challenging. This type of observer is applicable to model nonlinearities and constant feature gains. However, they are very sensitive to measurement noise, which is unavoidable in EHB. The first novelty of this study is that it compensates for the measurement noise using a filtered high-gain observer (FHGO) to ensure EHB state estimation. The proposed FHGO provides an estimate of the master cylinder pressure, motor current, and rotor speed from measurements of the rotor position. The second novelty is the design of an extremum-seeking (ES) optimization loop to adjust the FHGO gains online. The performance of the developed FHGO with ES-based online gain optimization was highlighted in the presence of model uncertainties and output measurement noise using a Matlab/Simulink simulation. The superiority of the FHGO (even with a fixed gain) over a standard high gain observer (SHGO) was also demonstrated.

Keywords: Electrohydraulic brake, filtered HGO, measurement noise, optimization, extremum-seeking, Lyapunov theory

1 Introduction

The severity of environmental pollution and the energy crisis have prompted greater focus on the research and development of electric vehicles (EVs) in many countries. Modern EVs are equipped with friction and regenerative braking systems to achieve better braking behavior and energy regeneration [1-2]. Electrohydraulic brakes (EHB) are superior to conventional hydraulic braking systems in terms of response time and performance. The EHB method described in Refs. [3-4] is the focus of this study. It consists of a DC electric motor-driven linear motion mechanism that presses the master cylinder directly to develop hydraulic pressure (Fig. 1).

In EHB operation, state variables such as the rotor position and master cylinder pressure are key information [5]. The EHBs are equipped with sensors to measure these variables. Obviously, the failure of one or more sensors leads to the malfunctioning of the EHB and possibly vehicle damage. One solution to make the EHB more reliable is to duplicate all the sensors. However, this approach is expensive and cumbersome. Furthermore, sensor measurements are very noisy in the present context. To overcome these limitations, we seek an alternative solution that consists of implementing a state observer instead of duplicating sensors. Thus, we reduce the cost of the EHB while preserving the reliability of the duplicated solution. Moreover, the observer-based solution was significantly less sensitive to noise.

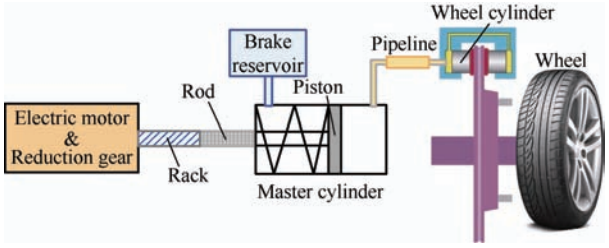

Fig. 1 EHB schematic diagram

Manuscript received May 26, 2023; revised August 11, 2023; accepted August 22, 2023. Date of publication December 31, 2023; date of current version October 9, 2023.
* Corresponding Author, E-mail: jamal.elbakkouri@ensem.ac.ma
Digital Object Identifier: 10.23919/CJEE.2023.000039

Compared with conventional hydraulic brakes, EHBs have been addressed much less in the control literature. The control design for these systems has been addressed using a proportional-integral-derivative (PID) controller [6] and sliding mode controller [4, 7]. In Ref. [8], the observer design for EHB was considered in the framework of output-feedback control. The proposed observer incorporates a simple estimator for hydraulic pressure in the EHB, neglecting any measurement noise or uncertainties in the model.

This study focuses on the observer design for an EHB system using the high-gain observer (HGO) design technique. HGOs feature a constant gain, making them simpler than varying-gain observers. However, its constant-gain nature raises the issue of selecting a gain value. Indeed, large gain values ensure rapid estimation error convergence in the absence of measurement noise. In the presence of noise, high gains amplify the effect of measurement noise and may deteriorate the stability of the observer. Another drawback of using a large gain value is peaking phenomenon [9]. Therefore, research on the design of filtered high-gain observers has been a long-standing issue [10-13]. Therefore, this study proposes a filtered high-gain observer (FHGO) for EHB systems. Design and stability analysis of FHGO using the Lyapunov theory are presented in this study. As will be proved later, the stability and convergence rate of the FHGO depend on the careful tuning of two parameters. To ensure good performance of the proposed observer, rather than manually choosing the tuning parameters of the FHGO, a real-time optimization of the two parameters was performed using the extremum seeking (ES) algorithm [14-16]. To address these issues, the following contributions were made.

(1) EHB model accounting for measurement noise. The proposed FHGO model considers measurement noise and estimates the rotor speed, motor current, and master cylinder pressure based solely on the measurement of the rotor position. This study considers the measurement noise overlaid on the measurable state throughout its development.

(2) Observability analysis. To ensure that the state variables of the EHB could be estimated, the observability property of the EHB was analyzed. Subsequently, a coordinate change by diffeomorphism to a uniformly observable form of the EHB model was performed to obtain a straightforward design for the FHGO.

(3) Standard high gain observer (SHGO). For pedagogical purposes, the SHGO (without a low-pass filter) for the EHB model in the presence of measurement noise was first designed. This design provides interesting insights into the filtered version of the design proposed later in this study.

(4) Filtered high-gain observer. The main contributions of this study are the design, stability analysis, and performance evaluation of the FHGO for EHB. The primary concept of the proposed FHGO is that a low-pass filter filters the output injection term before it is reinjected into the EHB observer. Thus, the asymptotic behavior of the proposed observer is preserved even in the presence of measurement noise.

(5) Online extremum seeking (ES) optimization of FHGO parameters. The choice of FHGO tuning parameters has proven to be complex. For simplicity and optimal tuning of the FHGO, the observer parameter selection problem was transformed into a real-time optimization problem using the ES.

The remainder of this paper is organized as follows. Section 2 describes the proposed EHB model. A problem statement is presented in Section 3. The EHB observability analysis, model transformation into a uniformly observable form, FHGO design, and stability analysis are explored in Section 4. In Section 5, online ES optimization of the FHGO tuning parameter is described. The performance validation of the proposed FHGO for the EHB model is highlighted through simulations using Matlab/Simulink in Section 6.

2 EHB modeling

In this section, we develop a mathematical model for the EHB [6, 17]. As shown in Fig. 1, the EHB consists mainly of an electric motor, worm gear, rack and pinion mechanism, master cylinder, braking pipe, and

wheel-cylinder mechanism. Models of the electrical, mechanical, and hydraulic subsystems are derived in the following subsections.

2.1 Electro-mechanical subsystem modeling

The DC motor can be modeled using a circuit with an ideal voltage generator that describes the back electromotive force (EMF) connected in series with an inductor and a resistor. The equations for the electrical system model are as follows

$$\begin{cases} L\dot{i} = u - Ri - e \\ e = k_e \omega_m \end{cases} \tag{1}$$

$$\begin{cases} J\dot{\omega}_m = T_m - T_l - k_{damp}\omega_m \\ T_m = k_e i \end{cases} \tag{2}$$

where u is the motor voltage; i is the motor current; e is the back EMF; J is the total moment of inertia of the motor and reduction gear; ω_m is the motor speed; T_m is the motor torque; T_l is the load torque owing to the master cylinder pressure; and k_{damp} is the motor damping coefficient. L, R, and k_e are the inductance of the motor, motor resistor, and back-EMF constant, respectively.

The dynamics of the mechanical part of the master cylinder can be described as follows

$$m_{mc}\ddot{x}_{mc} = F_l - A_{mc}P_{mc} \tag{3}$$

$$\begin{cases} F_l = r_g T_l \\ x_{mc} = \dfrac{1}{r_g}\theta_m \end{cases} \tag{4}$$

where m_{mc} is the mass of the master cylinder piston; x_{mc} is the position of the master cylinder piston; F_l is the force acting on the piston; θ_m is the rotor position; and r_g is the ratio of the total reduction mechanisms. p_{mc} is the pressure in the master cylinder and A_{mc} is its area.

Assumption 1: Acceleration element with mass in Eq. (3) can be eliminated owing to the minimal contribution of the inertial force of the master cylinder piston. Subsequently, Eq. (3) can be simplified as follows

$$F_l = A_{mc}P_{mc} \tag{5}$$

With the above assumption and using Eq. (4), Eqs. (2) and (4) can be expressed as follows

$$T_l = \frac{A_{mc}}{r_g} p_{mc} \tag{6}$$

$$J\dot{\omega}_m = k_e i - \frac{A_{mc}}{r_g} p_{mc} - k_{damp}\omega_m \tag{7}$$

2.2 Hydraulic subsystem modeling

The hydraulic subsystem modeling is discussed in this section. Using the theory of mass conservation, the dynamics of the master cylinder and wheel cylinder pressures are derived as follows

$$\begin{cases} \dot{p}_{mc} = \dfrac{\beta}{V_{mc}}\left(-q_{mc} + A_{mc}\dot{x}_{mc}\right) \\ V_{mc} = A_{mc}(s_{mc} - x_{mc}) \end{cases} \tag{8}$$

$$\begin{cases} \dot{p}_{wc} = \dfrac{\beta}{V_{wc}}\left(q_{wc} - A_{wc}\dot{x}_{wc}\right) \\ V_{wc} = A_{wc}x_{wc} \end{cases} \tag{9}$$

where β is the bulk modulus of the brake fluid; V_{mc} is the volume of fluid inside the master cylinder chamber; q_{mc} is the volumetric flow rate running out of the master cylinder chamber; s_{mc} is the master cylinder piston stroke; p_{wc} is the wheel cylinder pressure; V_{wc} is the volume of fluid in the caliper chamber; q_{wc} is the volumetric flow rate into the wheel cylinder; A_{wc} is the area of the wheel cylinder piston; and k_{wc} is the pad stiffness.

Applying Newton's second law to the wheel cylinder piston, the equation of motion is given as follows

$$m_{wc}\ddot{x}_{wc} = A_{wc}p_{wc} - k_{wc}(x_{wc} - x_{gap}) \tag{10}$$

where m_{wc}, x_{wc}, and x_{gap} represent the pad mass, position of the wheel cylinder piston, and air gap between the brake pad and brake disk, respectively.

Assumption 2: Owing to the small contribution of the inertial force of the wheel cylinder piston, acceleration with mass can be discarded, and Eq. (10) becomes

$$A_{wc}p_{wc} = k_{wc}(x_{wc} - x_{gap}) \tag{11}$$

Assumption 3: Ignoring pipeline dynamics and assuming linear flow, the hydraulic pressure drop in a circular pipeline can be expressed as follows

$$q_{mc} = q_{wc} = q = \frac{p_{mc} - p_{wc}}{k_{lk}} \tag{12}$$

where $k_{lk} = 8\nu\rho l_p / \pi r_p$ is the laminar flow coefficient,

ρ is the fluid density, ν is the cinematic viscosity of the brake fluid, l_p is the pipeline length, and r_p is the cross-sectional radius of the pipeline.

By using Eqs. (10)-(12), Eq. (8) and Eq. (9) can be rewritten as follows

$$\dot{p}_{mc}=\frac{\beta}{A_{mc}\left(s_{mc}-\frac{1}{r_g}\theta_m\right)}\left(\frac{1}{r_g}A_{mc}\omega_m-\frac{p_{mc}-p_{wc}}{k_{lk}}\right) \tag{13}$$

$$\dot{p}_{wc}=q\frac{k_{wc}}{A_{wc}^2}\left(1+\frac{p_{wc}+x_{gap}\frac{k_{wc}}{A_{wc}}}{\beta}\right)^{-1} \tag{14}$$

2.3 Observer design model of the EHB

According to Ref. [5], the propagation dynamics of the brake pressure waves were ignored. In other words, the master cylinder pressure was equal to the wheel cylinder pressure $(p_{mc}=p_{wc})$. Therefore, the wheel-cylinder dynamics in Eq. (14) can be disregarded.

Let the state vector $\boldsymbol{x}=[x_1\ \ x_2\ \ x_3\ \ x_4]^{\mathrm{T}}=[\theta_m\ \ \omega_m\ \ i\ \ p_{mc}]^{\mathrm{T}}$. The state representation of the EHB model (Eqs. (1), (7), (13)) can be expressed as follows

$$\begin{cases}\dot{x}(t)=f\left(u(t),x(t)\right)\\ y=h(x)+n(t)\end{cases} \tag{15}$$

$$f(x,u)=\begin{pmatrix}f_1(x,u)\\ f_2(x,u)\\ f_3(x,u)\\ f_4(x,u)\end{pmatrix}=\begin{pmatrix}x_2\\ \frac{-k_{damp}}{J}x_2+\frac{k_e}{J}x_3-\frac{A_{mc}}{J\cdot r_g}x_4\\ \frac{-k_e}{L}x_2-\frac{R}{L}x_3+\frac{u}{L}\\ \frac{\beta}{r_g\cdot s_{mc}-x_1}x_2\end{pmatrix} \tag{16}$$

where $h(x)=x_1$, $n(t)\in\mathbb{R}$ is the measurement noise of the measurable state x_1 and $u\in\mathbb{R}$ is the system input.

3 Filtered high-gain observer for EHB

3.1 Problem statement

The proposed state observer estimates the EHB state from the measurements of the motor voltage u (the input) and rotor position θ_m (the output), which are easily measured using an incremental encoder, often coupled with the rotor and gearbox. Unlike the extended Kalman observer, whose convergence is not guaranteed in general, and the sliding mode observer, which is subject to the chattering problem, the more efficient HGO is adopted in this study. HGO is very sensitive to measurement noise. Thus, we opted for filtered HGO in the EHB system in this study.

In SHGO (without a filtering action), the output correction term $(y-\hat{y})$ was reinjected directly into the EHB observer (Fig. 2). However, in the proposed FHGO, the idea is to filter the output injection term using a low-pass filter before reinjection into the observer (Fig. 3). Thus, the asymptotic convergence of the estimation error is always preserved, even in the presence of measurement noise.

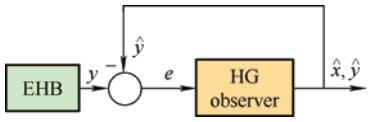

Fig. 2 Standard high-gain observer scheme

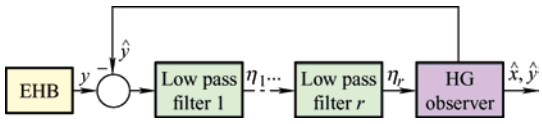

Fig. 3 Filtered high-gain observer scheme

As shown in the next section, for a given low-pass filter order *r*, the stability and convergence rate of the FHGO depend on careful tuning of two parameters. To guarantee good performance of the proposed observer, rather than manually adjusting the FHGO tuning parameters, real-time optimization of the two parameters by the ES algorithm was performed according to Fig. 4.

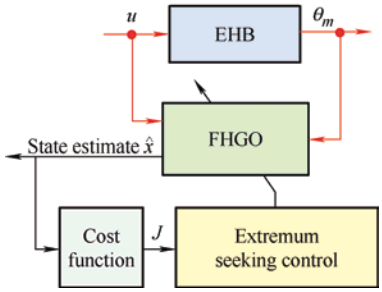

Fig. 4 Block diagram of the optimized FHGO

3.2 EHB observability analysis

Before designing the FHGO for the EHB model, it is necessary to analyze the observability of the system. An observability rank condition method based on the Lie derivative is used. Let the vector

$$\boldsymbol{O}(x)=[h(x),L_f^1h(x),L_f^2h(x),L_f^3h(x)]^{\mathrm{T}} \tag{17}$$

where $\boldsymbol{O}(x)$ is a mapping that constitutes the observation space, and $L_fh(x)$ is the Lie derivative of $h(x)$ with respect to the vector field $\boldsymbol{f}(x)=[f_1(x),f_2(x),f_3(x),f_4(x)]^{\mathrm{T}}$.

Proposition 1: Consider system in Eq. (15). The Jacobian of matrix $\boldsymbol{O}(x)$ is full rank, regardless of the state x variation. Thus, this system is observable almost everywhere.

Proof of Proposition 1. The observability of EHB can be assessed using the Jacobian of $\boldsymbol{O}(x)$. Applying the Lie derivative to Eq. (15), the matrix $\boldsymbol{O}(x)$ is obtained as follows

$$\boldsymbol{O}(x)=\begin{bmatrix} x_1 \\ x_2 \\ \dfrac{-k_{damp}}{J}x_2+\dfrac{k_e}{J}x_3-\dfrac{A_{mc}}{J\cdot r_g}x_4 \\ \alpha_1\dfrac{x_2}{r_gs_{mc}-x_1}+\alpha_2x_2+\alpha_3x_3+\alpha_4x_4+\dfrac{k_e}{JL}u \end{bmatrix} \tag{18}$$

where $\alpha_1=-A_{mc}\beta/Jr_g$, $\alpha_2=(k_{damp}/J)^2-k_e^2/JL$, $\alpha_3=-k_{damp}k_e/J^2-Rk_e/JL$, $\alpha_4=k_{damp}A_{mc}/r_gJ^2$.

The Jacobian of $\boldsymbol{O}(x)$ is expressed as follows

$$\boldsymbol{Jc}(x)=\frac{\partial\boldsymbol{O}(x)}{\partial x}=\begin{bmatrix} 1 & 0 & 0 & 0 \\ 0 & 1 & 0 & 0 \\ 0 & \dfrac{-k_{damp}}{J} & \dfrac{k_e}{J} & \dfrac{-A_{mc}}{Jr_g} \\ H_1 & H_2 & H_3 & H_4 \end{bmatrix} \tag{19}$$

where $H_1=\dfrac{\alpha_1\cdot x_2}{(r_gs_{mc}-x_1)^2}$, $H_2=\alpha_2+\dfrac{\alpha_1}{r_gs_{mc}-x_1}$, $H_3=\alpha_3$, and $H_4=\alpha_4$.

Clearly, the determinant of matrix $\boldsymbol{Jc}(x)$ is the following square matrix

$$\begin{bmatrix} \dfrac{k_e}{J} & \dfrac{-A_{mc}}{Jr_g} \\ H_3 & H_4 \end{bmatrix} \tag{20}$$

Thus

$$\det(\boldsymbol{Jc}(x))=\frac{k_e\cdot H_4}{J}+\frac{A_{mc}\cdot H_3}{r_gJ} \tag{21}$$

By replacing H_3 and H_4 with their expressions, we obtain

$$\det(\boldsymbol{Jc}(x))=-\left(\frac{2k_ek_{damp}A_{mc}}{J^2r_g}+\frac{k_eR}{J^2Lr_g}\right) \tag{22}$$

It is clear that: $\det(\boldsymbol{Jc}(x))\neq 0,\ \forall\, x\in\mathbb{R}^4$. This concludes the proof of Proposition 1.

3.3 Transformation to uniformly observable form

The EHB model is observable almost everywhere. A change in the coordinates can then convert it into a uniformly observable form [18]. This form allows for an easy and straightforward design of a high-gain observer.

Proposition 2: Consider the system in Eq. (15), it exists a diffeomorphism $\phi(x)$ defined as follows

$$\phi(x):\mathbb{R}^4\to\mathbb{R}^4, x\to z=\phi(x)=\begin{bmatrix} z_1 \\ z_2 \\ z_3 \\ z_4 \end{bmatrix}=\begin{bmatrix} \phi_1(x) \\ \phi_2(x) \\ \phi_3(x) \\ \phi_4(x) \end{bmatrix} \tag{23}$$

$\phi(x)$ transforms the system in Eq. (15) to a uniformly observable form expressed as follows

$$\begin{cases} \dot{z}(t)=\boldsymbol{A}z(t)+\boldsymbol{\varphi}\big(u(t),z(t)\big) \\ y(t)=\boldsymbol{C}z(t)+n(t) \end{cases} \tag{24}$$

where the matrices $\boldsymbol{A}$, $\boldsymbol{C}$ and $\boldsymbol{\varphi}(u,z)$ are given by the

$$\boldsymbol{A}=\begin{bmatrix} 0 & 1 & 0 & 0 \\ 0 & 0 & 1 & 0 \\ 0 & 0 & 0 & 1 \\ 0 & 0 & 0 & 0 \end{bmatrix},\boldsymbol{C}=\begin{bmatrix} 1 \\ 0 \\ 0 \\ 0 \end{bmatrix}^{\mathrm{T}},\boldsymbol{\varphi}(u,z)=\begin{bmatrix} \varphi_1(u,z_1) \\ \varphi_2(u,z_1,z_2) \\ \varphi_3(u,z_1,z_2,z_3) \\ \varphi_4(u,z) \end{bmatrix}$$

Proof of Proposition 2. Let $z_1=x_1$ be the system output. From Eq. (15), the derivative of z_1 is

$$\dot{z}_1=x_2=z_2 \tag{25}$$

According to Eq. (16), the dynamics of z_2 can be written as

$$\dot{z}_2=z_3+\varphi_2(u,z_1,z_2) \tag{26}$$

where $z_3=\dfrac{k_e}{J}x_3-\dfrac{A_{mc}}{Jr_g}x_4$, $\varphi_2(u,z_1,z_2)=\dfrac{-k_{damp}}{J}z_2$.

Similarly, the derivative of z_3 is obtained using Eq. (16) as

$$\dot{z}_3=z_4+\varphi_3(u,z_1,z_2,z_3) \tag{27}$$

where $z_4=\dfrac{-k_eR}{JL}x_3$, $\varphi_3(u,z_1,z_2,z_3)=\dfrac{-A_{mc}\beta}{Jr_g}\dfrac{z_2}{r_gs_{mc}-z_1}-\dfrac{k_e^2}{JL}z_2+\dfrac{k_e}{JL}u$.

Using Eq. (16) and Eq. (27), the derivative of z_4 is given as follow

$$\dot{z}_4=\frac{Rk_e^2}{JL^2}z_2-\frac{R}{L}z_4-\frac{Rk_e}{JL^2}u=\varphi_4(u,z) \tag{28}$$

Notice that from Eqs. (25)-(28), we can easily check the anti-shift form of matrix $\boldsymbol{A}$ and the triangular structure of the vector function $\boldsymbol{\varphi}(u,z)$. This result demonstrates that the canonical observability form of Eq. (24), and thus ends the proof of Proposition 2.

Remark 1: The original x-coordinates can be easily deduced from the z-coordinates as follows

$$\begin{cases} x_1 = z_1 \\ x_2 = z_2 \\ x_3 = -\dfrac{JL}{k_e R} z_4 \\ x_4 = -\dfrac{Jr_g}{A_{mc}} z_3 - \dfrac{JLr_g}{A_{mc} R} z_4 \end{cases}$$

3.4 FHGO for EHB in the presence of measurement noise

To make the observer design and analysis more realistic, the model developed in the previous subsection was augmented with measurement noise. Specifically, the EHB model can be rewritten as

$$\begin{cases} \dot{z}(t) = \boldsymbol{A}z(t) + \boldsymbol{\varphi}\big(u(t), z(t)\big) \\ y(t) = \boldsymbol{C}z(t) + n(t) = z_1 + n(t) \end{cases} \tag{29}$$

where $n(t)$ is the output measurement noise, which is assumed to be bounded, and its upper bound is denoted as $\delta_n > 0$. Matrices $\boldsymbol{A}$, $\boldsymbol{C}$, and $\boldsymbol{\varphi}(u,z)$ are defined in Proposition 2.

In the following, some definitions, notations, and assumptions are required for the convergence analysis of the observation error of the proposed observers.

$\lambda_{\min}(\cdot)$ (resp. $\lambda_{\max}(\cdot)$) denotes the smallest (resp. largest) eigenvalue. We define the diagonal matrix $\boldsymbol{\Delta}_\theta = diag(1, 1/\theta, 1/\theta^2, 1/\theta^3)$, with $\theta \geqslant 1$ as the scalar design parameter. Note that one can verify the following identities without difficulty

$$\begin{cases} \boldsymbol{\Delta}_\theta \boldsymbol{A} \boldsymbol{\Delta}_\theta^{-1} = \theta \boldsymbol{A} \\ \boldsymbol{C} \boldsymbol{\Delta}_\theta^{-1} = \boldsymbol{C} \end{cases} \tag{30}$$

Assumption 4: The state $z(t)$ is bounded, and a bound of it denoted ρ_z is known.

The angular position of the motor shaft $\theta_m = z_1$, angular speed $\omega_m = z_2$, current of the motor $i \propto z_4$, and master cylinder pressure $p_{mc} \propto (z_3 + z_4)$ are practically bounded. Then, Assumption 4 holds.

Property 1: Based on parameter values listed in Tab. 1 and that $z_1 \in [0, 2\pi]$, there exists $\varsigma > 0$ $\forall t$, $Gs_{mc} - z_1(t) > \varsigma$. Consequently, the functions φ_i of the vector function $\boldsymbol{\varphi}(u,z)$ are Lipschitz on the following convex compact set

$$\Omega = \left\{ z \in R^4, \ \|z\| \leqslant \rho_z \text{ and } Gs_{mc} - z_1 \succ \varsigma \right\}$$

3.4.1 SHGO for EHB in presence of measurement noise

In this subsection, the SHGO for EHB in the presence of measurement noise was designed for pedagogical purposes. This sheds light on the filtered-version design proposed in this study. The SHGO is represented by the block diagram in Fig. 2.

Considering the system EHB in the z-coordinates of Eq. (29), the following system Eq. (31) is the HGO of Eq. (29).

$$\dot{\hat{z}}(t) = \boldsymbol{A}\hat{z}(t) + \boldsymbol{\varphi}\big(u(t), \wp(\hat{z}(t))\big) - \boldsymbol{\theta}\boldsymbol{\Delta}_\theta^{-1}\boldsymbol{K}\big(\boldsymbol{C}\hat{z}(t) - y(t)\big) \tag{31}$$

where $\hat{z} \in \mathbb{R}^4$ is the state estimate of z, the mapping $\wp(\cdot)$ denotes the orthogonal projection on Ω, and $\boldsymbol{K} = (k_1, k_2, k_3, k_4)^{\mathrm{T}}$ is any vector such that the matrix $\overline{\boldsymbol{A}} \triangleq \boldsymbol{A} - \boldsymbol{K}\boldsymbol{C}$ is Hurwitz. Since the matrix $\overline{\boldsymbol{A}} \triangleq \boldsymbol{A} - \boldsymbol{K}\boldsymbol{C}$ is Hurwitz, there exists a 4×4 SPD matrix $\boldsymbol{P}$ such that

$$\boldsymbol{P}\overline{\boldsymbol{A}} + \overline{\boldsymbol{A}}^{\mathrm{T}}\boldsymbol{P} = -2I_4 \tag{32}$$

The estimation error was introduced as $\boldsymbol{e} = (e_1, e_1, e_3, e_4)^{\mathrm{T}} = \hat{z} - z$. Subsequently, we obtain the following result.

Proposition 3: Assume that the EHB system in Eq. (29) satisfies assumption 4: A real scalar θ_0 exists such that for $\theta > \theta_0$, Eq. (31) holds, and is the global exponential observer for the system in Eq. (29) in the sense that

$$\|e(t)\| \leqslant \sigma\theta^3 \|e(0)\| \exp\left(-\frac{\theta}{2\lambda_{\max}(P)} t \right) + 2\sigma\lambda_{\max}(P)\theta^3\delta_n \tag{33}$$

where $\sigma = \sqrt{\lambda_{\max}(P)/\lambda_{\min}(P)}$.

Proof of Proposition 3. Defining the estimation error as $\boldsymbol{e} = (e_1, e_1, e_3, e_4)^{\mathrm{T}} = \hat{z} - z$, its dynamics are given by

$$\dot{e} = \big(\boldsymbol{A} - \boldsymbol{\theta}\boldsymbol{\Delta}_\theta^{-1}\boldsymbol{K}\boldsymbol{C}\big)\boldsymbol{e} + \big(\boldsymbol{\varphi}\big(u, \wp(\hat{z})\big) - \boldsymbol{\varphi}\big(u,z\big)\big) + \boldsymbol{\theta}\boldsymbol{\Delta}_\theta^{-1}\boldsymbol{K}n(t) \tag{34}$$

Let introduce coordinate changes

$$\overline{e} = \boldsymbol{\Delta}_\theta \boldsymbol{e} \tag{35}$$

Using Eq. (30), it is verified that the new error $\overline{e}$ is governed by the following equation

$$\dot{\bar{e}} = \boldsymbol{\theta}\bar{\boldsymbol{A}}\bar{\boldsymbol{e}} + \boldsymbol{\Delta}_\theta\left(\boldsymbol{\varphi}\left(u,\wp(\hat{z})\right)-\boldsymbol{\varphi}\left(u,z\right)\right)+\boldsymbol{\theta}\boldsymbol{K}n(t) \quad (36)$$

Let $V(\bar{\boldsymbol{e}})=\bar{\boldsymbol{e}}^{\mathrm{T}}\boldsymbol{P}\bar{\boldsymbol{e}}$ be a Lyapunov function for the system in Eq. (36), and $\boldsymbol{P}$ verifies Eq. (32). By differentiating $V(\bar{\boldsymbol{e}})$ with respect to time, we obtain

$$\dot{V}(\bar{\boldsymbol{e}}) \leqslant -2\boldsymbol{\theta}\left\|\bar{\boldsymbol{e}}\right\|^2 + 2\left\|\bar{\boldsymbol{e}}^{\mathrm{T}}\boldsymbol{P}\right\|\times$$
$$\left(\left\|\boldsymbol{\Delta}_\theta\left(\boldsymbol{\varphi}\left(u,\wp(\hat{z})\right)-\boldsymbol{\varphi}\left(u,z\right)\right)\right\|+\boldsymbol{\theta}\left\|\boldsymbol{K}n(t)\right\|\right) \quad (37)$$

Using Assumption 4 and the triangular structure of the vector function $\boldsymbol{\varphi}(u,z)$, we apply the mean-value theorem

$$2\left\|\bar{\boldsymbol{e}}^{\mathrm{T}}\boldsymbol{P}\right\|\left\|\boldsymbol{\Delta}_\theta\left(\boldsymbol{\varphi}\left(u,\wp(\hat{z})\right)-\boldsymbol{\varphi}\left(u,z\right)\right)\right\| \leqslant 2\ell\lambda_{\max}(\boldsymbol{P})\left\|\bar{\boldsymbol{e}}\right\|^2 \quad (38)$$

where ℓ is a positive real constant that does not depend on the θ ($\theta \geqslant 1$).

By using Eq. (30), one has

$$2\theta\left\|\bar{\boldsymbol{e}}^{\mathrm{T}}\boldsymbol{P}\right\|\left\|\boldsymbol{K}n(t)\right\| \leqslant 2\theta\delta_n\lambda_{\max}(p)\left\|\bar{\boldsymbol{e}}\right\| \quad (39)$$

By combining Eqs. (37)-(39), we obtain

$$\dot{V}(\bar{\boldsymbol{e}}) \leqslant -2\left(\theta-\ell\lambda_{\max}(\boldsymbol{P})\right)\left\|\bar{\boldsymbol{e}}\right\|^2 + 2\lambda_{\max}(\boldsymbol{P})\theta\delta_n\left\|\bar{\boldsymbol{e}}\right\| \quad (40)$$

Let θ be sufficiently large enough so that $2\left(\theta-\ell\lambda_{\max}(p)\right)>\theta$, that is, $\theta>\theta_0=2\ell\lambda_{\max}(\boldsymbol{P})>0$.

From $\lambda_{\min}(\boldsymbol{P})\left\|\bar{\boldsymbol{e}}\right\|^2 \leqslant V(\bar{\boldsymbol{e}}) \leqslant \lambda_{\max}(\boldsymbol{P})\left\|\bar{\boldsymbol{e}}\right\|^2$, inequality (40) becomes

$$\dot{V}(\bar{\boldsymbol{e}}) \leqslant -\frac{\theta}{\lambda_{\max}(\boldsymbol{P})}V(\bar{\boldsymbol{e}}) + \frac{2\lambda_{\max}(\boldsymbol{P})}{\sqrt{\lambda_{\min}(\boldsymbol{P})}}\theta\delta_n\sqrt{V(\bar{\boldsymbol{e}})} \quad (41)$$

It can be easily verified that Eq. (41) implies

$$\frac{\mathrm{d}}{\mathrm{d}t}\sqrt{V(\bar{\boldsymbol{e}})} \leqslant -\frac{\theta}{2\lambda_{\max}(\boldsymbol{P})}\sqrt{V(\bar{\boldsymbol{e}})} + \frac{\lambda_{\max}(\boldsymbol{P})}{\sqrt{\lambda_{\min}(\boldsymbol{P})}}\theta\delta_n \quad (42)$$

By applying the comparison lemma [19], we obtain

$$\sqrt{V\left(\bar{e}(t)\right)} \leqslant \sqrt{V\left(\bar{e}(0)\right)}\exp\left(-\frac{\theta}{2\lambda_{\max}}t\right) + \frac{2\lambda_{\max}^2(\boldsymbol{P})}{\sqrt{\lambda_{\min}(\boldsymbol{P})}}\delta_n \quad (43)$$

which yields

$$\left\|\bar{e}(t)\right\| \leqslant \sigma\left\|\bar{e}(0)\right\|\exp\left(-\frac{\theta}{2\lambda_{\max}(\boldsymbol{P})}t\right) + 2\sigma\lambda_{\max}(\boldsymbol{P})\delta_n \quad (44)$$

where $\sigma=\sqrt{\lambda_{\max}(\boldsymbol{P})/\lambda_{\min}(\boldsymbol{P})}$.

From Eq. (35), one has $\left\|\bar{e}\right\| \leqslant \left\|e\right\| \leqslant \theta^3\left\|\bar{e}\right\|$. Subsequently, from Eq. (44), we obtain Eq. (33). This concludes the proof of Proposition 3.

From Eq. (33), it is seen that if $\delta_n=0$ (absence of measurement noise), the observation error converges exponentially to zero for a large enough θ. In practice, measurement noise is generally present, making high values of θ highly problematic. Indeed, inequality Eq. (33) shows that the mapping "measurement noise $\rightarrow$ estimation error" is input-to-state stable with a gain proportional to θ^3. Therefore, high values of θ lead to larger estimation error.

To better analyze the asymptotic behavior of the estimation error, the measurement noise was modeled using a finite Fourier series

$$n(t)=\sum_{i=1}^{N} n_i\sin\left(\frac{\omega_{si}}{\varepsilon}t+\vartheta_i\right) \quad (45)$$

where $N>0$ is any positive integer, the parameter $0<\varepsilon\ll 1$ shifts the base frequencies ω_{si} to high frequencies (for sufficiently small ε, the measurement noise Eq. (45) exhibits high-frequency behavior). The real quantities $n_i>0$ and ϑ_i denote the amplitude and phase of each component, respectively. Using these notations, the steady-state estimation error is bounded as follows

$$\limsup_{t\to\infty}\left\|e_i(t)\right\| \leqslant \varepsilon\varrho\theta^i\delta_n \qquad i=1,\cdots,4 \quad (46)$$

where some scalar $\varrho>0$ independent on θ. Again, this shows that: the higher θ, the larger the state estimation error components.

3.4.2 FHGO for EHB: Design and analysis

To overcome the performance limitations of the SHGO, we will design and analyze an FHGO for the EHB model. As shown in Fig. 3, the output-injection term was filtered using a low-pass filter before being reinjected into the EHB observer. Thus, the asymptotic behavior of the resulting observer in the absence of measurement noise is preserved in the presence of measurement noise.

The FHGO of the system in Eq. (29) is defined as follows

$$\begin{cases}\dot{\hat{z}}(t)=\boldsymbol{A}\hat{z}(t)+\boldsymbol{\varphi}\left(u(t),\wp\left(\hat{z}(t)\right)\right)-\theta\boldsymbol{\Delta}_\theta^{-1}\boldsymbol{G}\boldsymbol{B}_r^{\mathrm{T}}\eta(t)\\ \dot{\eta}(t)=-\frac{\theta}{\kappa}\left(\boldsymbol{I}_r-\boldsymbol{A}_r^{\mathrm{T}}\right)\eta(t)+\frac{\theta}{\kappa}\boldsymbol{C}_r^{\mathrm{T}}\left(\boldsymbol{C}\hat{z}(t)-y(t)\right)\end{cases} \quad (47)$$

where $\eta(0)=0$ and arbitrary $z(0)\in\Omega$, and $\hat{z}(0)\in\boldsymbol{R}^4$, where $r\in\mathbb{Z}^{*+}$ is the relative degree of the low-pass filter. The filter is parameterized by the high-gain parameter θ of the observer and a second parameter $\kappa>0$. The vector $\boldsymbol{G}=(G_1,G_2,G_3,G_4)^{\mathrm{T}}$ is arbitrarily selected such that $\boldsymbol{A}-\boldsymbol{G}\boldsymbol{C}$ is a Hurwitz vector.

Matrices $\boldsymbol{A}_r$, $\boldsymbol{B}_r$, $\boldsymbol{C}_r$, and $\boldsymbol{\eta}$ are defined as follows

$$\begin{cases} \boldsymbol{A}_r = \begin{bmatrix} 0_{r-1,1} & I_{r-1} \\ 0 & 0_{1-r,1} \end{bmatrix} \\ \boldsymbol{B}_r = \begin{bmatrix} 0_{r-1,1} \\ 1 \end{bmatrix} \\ \boldsymbol{C}_r = \begin{bmatrix} 1 & 0_{1-r,1} \end{bmatrix} \\ \boldsymbol{\eta} = \begin{bmatrix} \eta_1 & \cdots & \eta_r \end{bmatrix}^{\mathrm{T}} \end{cases}$$

We define the transformed state-estimation error as $\bar{e} = \boldsymbol{\Delta}_\theta e = \boldsymbol{\Delta}_\theta(\hat{z} - z)$. Assuming that θ varies slowly such that its derivative is neglected, it follows from Eqs. (29), (30), and (47), $\bar{e}$ is governed by the following equation

$$\dot{\bar{e}}(t) = \theta \boldsymbol{A}\bar{e}(t) + \boldsymbol{\Delta}_\theta\left(\boldsymbol{\varphi}\left(u, \wp(\hat{z})\right) - \boldsymbol{\varphi}(u, z)\right) - \theta \boldsymbol{G}\boldsymbol{B}_r^{\mathrm{T}}\eta(t) \tag{48}$$

Let introduce the augmented state vector $\boldsymbol{\xi} = [\bar{\boldsymbol{e}}^{\mathrm{T}}, \boldsymbol{\eta}^{\mathrm{T}}]^{\mathrm{T}}$. It follows from Eqs. (47) and (48) that this vector can be expressed as follows

$$\dot{\boldsymbol{\xi}}(t) = \theta \boldsymbol{F}(\kappa)\boldsymbol{\xi}(t) + \boldsymbol{\psi}(u, \hat{z}, z) - \boldsymbol{\Theta}\left(n(t)\right) \tag{49}$$

where

$$\boldsymbol{F}(\kappa) = \begin{bmatrix} \boldsymbol{A} & -\boldsymbol{G}\boldsymbol{B}_r^{\mathrm{T}} \\ \dfrac{1}{\kappa}\boldsymbol{C}_r^{\mathrm{T}}\boldsymbol{C} & -\dfrac{1}{\kappa}\left(I_r - \boldsymbol{A}_r^{\mathrm{T}}\right) \end{bmatrix}, \boldsymbol{\Theta}\left(n(t)\right) = \begin{bmatrix} 0_{4,1} \\ \dfrac{\theta}{\kappa}\boldsymbol{C}_r^{\mathrm{T}} n(t) \end{bmatrix},$$

and $\boldsymbol{\psi}(u, \hat{z}, z) = \begin{bmatrix} \boldsymbol{\Delta}_\theta\left(\boldsymbol{\varphi}\left(u, \wp(\hat{z})\right) - \boldsymbol{\varphi}(u, z)\right) \\ 0_{r,1} \end{bmatrix}$

As $\boldsymbol{A} - \boldsymbol{G}\boldsymbol{C}$ is Hurwitz, it follows that for any $r \in \mathbb{Z}^{*+}$, there exists $\kappa_0 > 0$ such that for each $\kappa \in [0, \kappa_0]$, $\boldsymbol{F}(\kappa)$ is Hurwitz. Therefore, there exists an SPD matrix $\boldsymbol{Q}$ such that

$$\boldsymbol{Q}\boldsymbol{F}(\kappa) + \boldsymbol{F}(\kappa)^{\mathrm{T}}\boldsymbol{Q} = -2I_{r+4} \tag{50}$$

The main results of this study are as follows.

Theorem 1: Consider FHGO in Eq. (47) to the EHB model in Eq. (29), subject to Assumption 4 and Property 1. There exists $\kappa_0 > 0$ such that for each $\kappa \in [0, \kappa_0]$, a real scalar θ_0 exists such that for $\theta > \theta_0$, the observer of Eq. (47), when applied to the system in Eq. (29) yields the following

$$\left\|e(t)\right\| \leqslant \mu\theta^3 \left\|e(0)\right\| \exp\left(-\frac{\theta}{2\lambda_{\max}(\boldsymbol{Q})}t\right) + 2\mu\lambda_{\max}(\boldsymbol{Q})\frac{\theta^3}{\kappa}\delta_n \tag{51}$$

where $\mu = \sqrt{\lambda_{\max}(\boldsymbol{Q})/\lambda_{\min}(\boldsymbol{Q})}$.

Proof of Theorem 1. Consider the Lyapunov candidate function

$$V(\xi) = \boldsymbol{\xi}^{\mathrm{T}}\boldsymbol{Q}\boldsymbol{\xi} \tag{52}$$

The derivative of $V(\xi)$ is as

$$\dot{V}(\xi) = \theta\boldsymbol{\xi}^{\mathrm{T}}\left[\boldsymbol{Q}\boldsymbol{F}(\kappa) + \boldsymbol{F}(\kappa)^{\mathrm{T}}\boldsymbol{Q}\right]\boldsymbol{\xi} + 2\boldsymbol{\xi}^{\mathrm{T}}\boldsymbol{Q}\left[\psi(u, \hat{z}, z) - \boldsymbol{\Theta}\left(n(t)\right)\right] \tag{53}$$

Using Eq. (50), one has

$$\dot{V}(\xi) \leqslant -2\theta\left\|\xi\right\|^2 + 2\left\|\boldsymbol{\xi}^{\mathrm{T}}\boldsymbol{Q}\right\| \times \left(\left\|\boldsymbol{\Delta}_\theta\left(\boldsymbol{\varphi}\left(u, \wp(\hat{z})\right) - \boldsymbol{\varphi}(u, z)\right)\right\| + \frac{\theta}{\kappa}\left\|\boldsymbol{C}_r^{\mathrm{T}} n(t)\right\|\right) \tag{54}$$

According to Assumption 4, the triangular structure of the vector function $\boldsymbol{\varphi}(u, z)$, the mean value theorem, and the identities in Eq. (30), we can verify that

$$2\left\|\bar{\boldsymbol{e}}^{\mathrm{T}}\boldsymbol{Q}\right\|\left\|\boldsymbol{\Delta}_\theta\left(\boldsymbol{\varphi}\left(u, \wp(\hat{z})\right) - \boldsymbol{\varphi}(u, z)\right)\right\| \leqslant 2\ell\lambda_{\max}(\boldsymbol{Q})\left\|\bar{e}\right\|^2 \tag{55}$$

$$2\theta\left\|\bar{\boldsymbol{e}}^{\mathrm{T}}\boldsymbol{Q}\right\|\left\|Kn(t)\right\| \leqslant 2\theta\delta_n\lambda_{\max}(\boldsymbol{Q})\left\|\bar{e}\right\| \tag{56}$$

where ℓ is a positive constant that does not depend on θ for $\theta \geqslant 1$.

Using Eqs. (55)-(56) and the inequality $\left\|\bar{e}\right\| \leqslant \left\|\xi\right\|$, we obtain

$$\dot{V}(\xi) \leqslant -2\left(\theta - \ell\lambda_{\max}(\boldsymbol{Q})\right)\left\|\xi\right\|^2 + 2\lambda_{\max}(\boldsymbol{Q})\frac{\theta}{\kappa}\delta_n\left\|\xi\right\| \tag{57}$$

Now, let θ be sufficiently high, such that $2\left(\theta - \ell\lambda_{\max}(\boldsymbol{Q})\right) > \theta$, that is $\theta > \theta_0 = 2\ell\lambda_{\max}(\boldsymbol{Q}) > 0$. By doing so, and using $\lambda_{\min}(\boldsymbol{Q})\left\|\bar{e}\right\|^2 \leqslant V(\bar{e}) \leqslant \lambda_{\max}(\boldsymbol{Q})\left\|\bar{e}\right\|^2$, we obtain

$$\dot{V}(\xi) \leqslant -\frac{\theta}{\lambda_{\max}(\boldsymbol{Q})}V(\xi) + 2\frac{\lambda_{\max}(\boldsymbol{Q})}{\sqrt{\lambda_{\min}(\boldsymbol{Q})}}\frac{\theta}{\kappa}\delta_n\sqrt{V(\xi)} \tag{58}$$

Eq. (58) can be rewritten as

$$\frac{\mathrm{d}}{\mathrm{d}t}\sqrt{V(\xi)} \leqslant -\frac{\theta}{2\lambda_{\max}(\boldsymbol{Q})}\sqrt{V(\xi)} + \frac{\lambda_{\max}(\boldsymbol{Q})}{\sqrt{\lambda_{\min}(\boldsymbol{Q})}}\frac{\theta}{\kappa}\delta_n \tag{59}$$

Using the comparison lemma [19], we obtain

$$\sqrt{V(\xi(t))} \leqslant \sqrt{V(\xi(0))}\exp\left(\frac{-\theta}{2\lambda_{\max}(\boldsymbol{Q})}t\right) + \frac{2\lambda_{\max}^2(\boldsymbol{Q})}{\sqrt{\lambda_{\min}(\boldsymbol{Q})}}\frac{\delta_n}{\kappa} \tag{60}$$

Using Eq. (52), Eq. (60) leads to

$$\left\|\xi(t)\right\| \leqslant \mu\left\|\xi(0)\right\|\exp\left(-\frac{\theta}{2\lambda_{\max}(\boldsymbol{Q})}t\right) + 2\mu\lambda_{\max}(\boldsymbol{Q})\frac{\delta_n}{\kappa} \tag{61}$$

The results of Theorem 1 follow from Eq. (61),

using the initial condition $\eta(0)=0$ and the inequalities $\|e\| \leqslant \theta^3 \|\bar{e}\| \leqslant \theta^3 \|\xi\|$ and $\|\xi\|^2 \leqslant \|\bar{e}\|^2 + \|\eta\|^2$. This completes the proof of Theorem 1.

In the case of a high-frequency measurement noise $n(t)$ similar to Eq. (45), the steady-state estimation error is bounded as follows [20]

$$\limsup_{t\to\infty} \|e_i(t)\| \leqslant \varrho \varepsilon^{r+1} \left(\frac{\theta}{\kappa}\right)^r \theta^i \delta_n \qquad i=1,\cdots,4 \tag{62}$$

where ϱ is a positive scalar that is independent of θ and κ.

It follows from Eq. (62) that with a judicious choice of θ and κ according to Theorem 1, the norm of the estimation error converges to a neighborhood of zero. The convergence rate can be made arbitrarily high by tuning r (because of the term ε^{r+1}). Unlike the performance of the SHGO (Eq. (46)), the performance of FHGO (Eq. (62)) contains the term ε^{r+1} (with $\varepsilon \approx 0$ used for high-frequency measurement noise). This term compensates for the negative effects of the $(\theta/\kappa)^r$.

4 Online ES tuning of θ and κ

In the presence of high-frequency measurement noise, a key issue is how to select the parameters θ and κ of the FHGO observer of Eq. (47). On the one hand, θ should be large enough to ensure a fast convergence of the estimation error to zero (in the noise-free case); on the other, a large value of θ entails noise effect amplification on the state estimation error. A high value of θ may also cause "peaking phenomenon" during the transient period. It turns out that the choice of θ should meet a compromise between fast convergence rate, sensitivity to measurement noise, and peaking phenomenon. Furthermore, Eq. (62) shows that a high correlation exists between κ, θ, and the low-pass filter order r. By Theorem 1, κ should not be too large.

Clearly, making a satisfactory a priori choice of the FHGO parameters is a complex task. Therefore, we sought the online tuning of these parameters. To this end, a real-time optimization problem involving observer parameters was defined and solved using an extremum seeking (ES) approach. One of the main features of this real-time adaptive optimization technique is its model-free nature. Here, a multivariable Newton-based ES was used (while maintaining a fixed LPF order r) (Fig. 5). The convergence rate in ES using Newton's method is user-assignable and does not depend on the unknown Hessian of the cost function, unlike in gradient-based ES [14].

4.1 Cost function selection

The selection of a suitable cost function is crucial. One possible choice is the quadratic function $e_1^2 = (\hat{z}_1 - z_1)^2 = (\hat{\theta}_m - \theta_m)^2$. However, this function is only weakly sensitive to measurement noise. Indeed, Eq. (62) shows that the convergence to zero of e_1^2 does not necessarily imply convergence to zero for other estimation errors. In fact, $e_4 = \hat{z}_4 - z_4$ is most affected by the measurement noise and peaking phenomena (owing to θ^4 in Eq. (62)). Based on these observations and Remark 1, the following cost function was considered

$$J(\theta,\kappa) = (\hat{x}_4 - x_4)^2 = (\hat{p}_{mc} - p_{mc})^2 \tag{63}$$

Because the master cylinder pressure p_{mc} was unmeasurable, it was replaced by the reference p_{mc_ref} (Fig. 5). A PID controller is used in a state feedback control to ensure that p_{mc} tracks p_{mc_ref}.

4.2 Multivariable newton-based ES

From Remark 1, Eq. (63) can be expressed as

$$J(\boldsymbol{\varpi}) = \left(c_1\left(e_3 + c_2 e_4\right)\right)^2 \tag{64}$$

where $\boldsymbol{\varpi} = (\theta,\kappa)^{\mathrm{T}}$, $c_1 = Jr_g / A_{mc}$, and $c_2 = L/R$.

Property 2: From Eq. (62) and according to Theorem 1, there exists an $\boldsymbol{\varpi}^* = (\theta^*,\kappa^*)^{\mathrm{T}}$ such that

$$\frac{\partial J}{\partial \boldsymbol{\varpi}}\left(\boldsymbol{\varpi}^*\right) = 0 \tag{65}$$

$$\frac{\partial^2 J}{\partial \boldsymbol{\varpi}^2}\left(\boldsymbol{\varpi}^*\right) = \boldsymbol{H} < 0,\ \boldsymbol{H} = \boldsymbol{H}^{\mathrm{T}} \tag{66}$$

where $\boldsymbol{H}$ is the Hessian.

The perturbation signals and matrix (Fig. 5) are defined as follows

$$\boldsymbol{S}(t) = a\left[\sin(\omega_1 t),\ \sin(\omega_2 t)\right]^{\mathrm{T}} \tag{67}$$

$$\boldsymbol{M}(t) = \frac{2}{a}\left[\sin(\omega_1 t),\ \sin(\omega_2 t)\right]^{\mathrm{T}} \tag{68}$$

$$\boldsymbol{N}(t) = \begin{bmatrix} \frac{16}{a^2}\left(\sin^2(\omega_1 t) - \frac{1}{2}\right) & \frac{4}{a^2}\sin(\omega_1 t)\sin(\omega_2 t) \\ \frac{4}{a^2}\sin(\omega_1 t)\sin(\omega_2 t) & \frac{4}{a^2}\left(\sin^2(\omega_2 t) - \frac{1}{2}\right) \end{bmatrix} \tag{69}$$

where a denotes a real number. The gain $\boldsymbol{D}=diag(d_1, d_2)$, frequencies ω_1, ω_2, and ω_r are chosen as follows

$$\omega_1=\omega\breve{\omega}_1=O(\omega) \tag{70}$$

$$\omega_2=\omega\breve{\omega}_2=O(\omega) \tag{71}$$

$$\breve{\omega}_1\neq\breve{\omega}_2 \tag{72}$$

$$\omega_r=\omega\omega_r=\omega\delta\breve{\omega}_r=O(\omega\delta) \tag{73}$$

$$\boldsymbol{D}=\omega\bar{D}=\omega\delta\breve{D}=O(\omega\delta) \tag{74}$$

where ω and δ are small positive constants, $\breve{\omega}_1$ and $\breve{\omega}_2$ are rational numbers, $\breve{\omega}_r$ is $O(1)$ positive constant, $\boldsymbol{D}$ is a diagonal matrix with $O(1)$ positive elements.

In Fig. 5, the dashed part provides the Hessian estimation. Without this part, the optimization scheme reduces to the gradient-based ES. The demodulation by low-pass filtering of the product $(J(\varpi)-\gamma)N(t)$ gives the estimated $\hat{H}$. A direct inversion of the Hessian $\boldsymbol{H}$ can be problematic when $\hat{H}$ is close to singularity or to be indefinite. To get around this issue, the following Riccati equation is used to get an estimate of the inverse of $\hat{H}$.

$$\dot{\Gamma}=\omega_r\Gamma-\omega_r\Gamma\hat{H}\Gamma \tag{75}$$

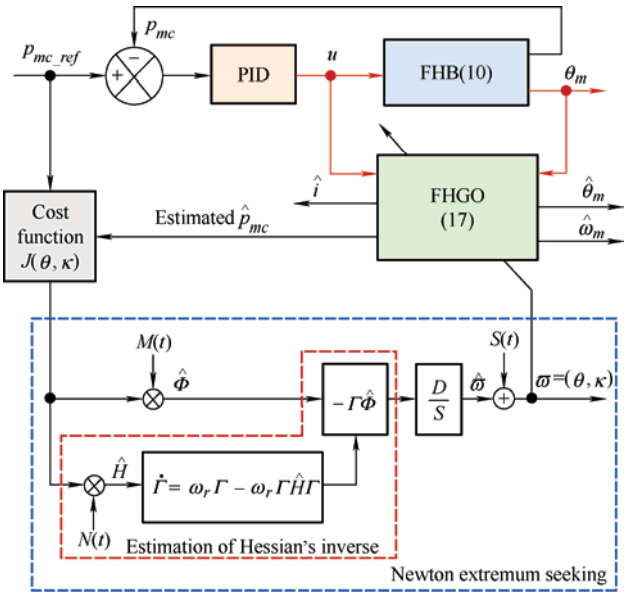

Fig. 5 Schematic of Newton's ES strategy for optimizing FHGO parameters

The Riccati equation has two steady-state solutions, $\Gamma_1^*=0_{2\times2}$ and $\Gamma_2^*=\hat{H}^{-1}$. Owing to $\omega_r>0$, the first solution is unstable, whereas the second is locally exponentially stable (linearization of Eq. (75) around $\hat{H}^{-1}$ is the Jacobian $-\omega_r I_{2\times2}$). Thus, the Riccati equation converges to the real value of the Hessian matrix inverse $\boldsymbol{H}^{-1}$ after the transient.

From Fig. 5, the dynamics of the estimated $\hat{\varpi}$ are given by

$$\dot{\hat{\varpi}}=-D\Gamma M(t)J(\varpi) \tag{76}$$

The gradient-based ES (Fig. 5, without the dashed part) was verified using Eq. (76), the dynamics of estimation error $\tilde{\varpi}=\hat{\varpi}-\varpi^*$ are $\dot{\tilde{\varpi}}=DH\tilde{\varpi}$. In Newton-based ES, the estimation error becomes $\dot{\tilde{\varpi}}=-D\Gamma H\tilde{\varpi}$, which is independent of the Hessian $\boldsymbol{H}$ (because $\boldsymbol{\Gamma}=\boldsymbol{H}^{-1}$).

The Taylor series expansion of the cost function $J(\varpi)$ around ϖ^* yields the following second approximation

$$J(\varpi)=J(\varpi^*)+\frac{1}{2}(\varpi-\varpi^*)^{\mathrm{T}}H(\varpi-\varpi^*) \tag{77}$$

Considering Eq. (77), the average closed-loop system is expressed using the error variables $\tilde{\varpi}=\hat{\varpi}-\varpi^*$ and $\tilde{\Gamma}=\boldsymbol{\Gamma}-\boldsymbol{H}^{-1}$ as follows

$$\dot{\tilde{\varpi}}_{av}=-D\tilde{\varpi}_{av}-D\underbrace{\tilde{\Gamma}_{av}H\tilde{\varpi}_{av}}_{\text{Quadratic}} \tag{78}$$

$$\dot{\tilde{\Gamma}}_{av}=-\omega_r\tilde{\Gamma}_{av}-\omega_r\underbrace{\tilde{\Gamma}_{av}H\tilde{\Gamma}_{av}}_{\text{Quadratic}} \tag{79}$$

Linearizing the system of Eqs. (78) and (79) around the stable equilibrium leads to a linear approximation

$$\begin{bmatrix}\dot{\tilde{\varpi}}_{av,eq}\\ \dot{\tilde{\Gamma}}_{av,eq}\end{bmatrix}=\begin{bmatrix}-D & 0_{2\times2}\\ 0_{2\times2} & -\omega_r\end{bmatrix}\begin{bmatrix}\tilde{\varpi}_{av,eq}\\ \tilde{\Gamma}_{av,eq}\end{bmatrix} \tag{80}$$

Clearly, system Eq. (80) is exponentially stable because its eigenvalues are negative owing to Eqs. (73)-(74). The closed-loop system expressed in Eqs. (78)-(79) are locally exponentially stable, and the convergence rate is tunable through the parameters D and ω_r.

5 Simulation results

5.1 Simulation protocol

To validate the performance of the FHGO proposed in Eq. (47) to the EHB model in Eq. (29), simulation tests were performed using Matlab/Simulink with the sampling time $T=50\ \mu s$. The various parameters of the EHB model are given the numerical values of Tab. 1. The gains of SHGO and FHGO are chosen

such that the matrices $\boldsymbol{A}-\boldsymbol{KC}$ and $\boldsymbol{A}-\boldsymbol{GC}$ are Hurwitz matrices and are given the values $\boldsymbol{K}=\boldsymbol{G}=(5,\ 8,\ 11,\ 7)^{\mathrm{T}}$.

Tab. 1 EHB model parameter numerical values

Description	Value
Inductance of the motor L/H	16×10^{-5}
Motor resistor R/Ω	0.9
Back EMF constant k_e/(N • m/A)	0.05
Gear's total moment of inertia J/(kg/m^2)	0.001 75
Motor damping coefficient k_{damp}/(N • ms/rad)	0.001
Area of master cylinder A_{mc}/m^2	0.000 35
Ratio of total reduction mechanism r_g/m^{-1}	2 330
Bulk modulus of the brake fluid β/MPa	1.6×10^3
Master cylinder piston stroke s_{mc}/mm	40

Two simulation results are obtained to highlight the performance of the proposed FHGO in the presence of various noise signals.

For the results presented in Subsections 5.2 to 5.4, the measurement noise has been generated by considering Eq. (45) using $N=2$, $\varepsilon=0.001$, $\omega_{s1}=1$, $\omega_{s2}=\sqrt{3}$, $n_1=0.15$, and $n_2=0.25$. It is the sum of two high-frequency sinusoidal signals. Fig. 6 shows the noisy nature of the observer output θ_m.

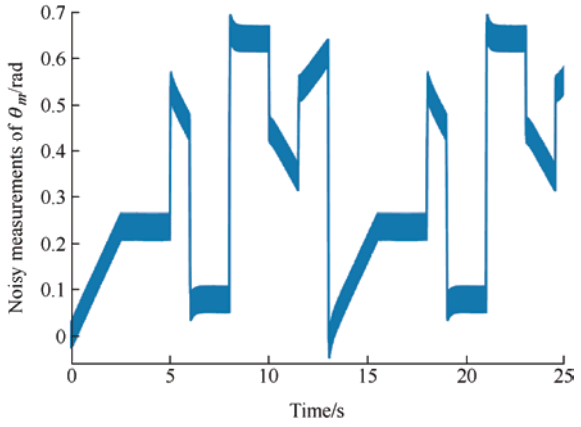

Fig. 6 Noisy measurement of θ_m (sinusoidal type)

In Subsection 5.5, simulation tests are performed considering Gaussian noise with a variance of 0.000 5. In that case, the noisy measurements of θ_m is shown in Fig. 7.

Note that for all simulation tests, the signal $\upsilon(t)=0.01\cos(50t)$ has been added on the right-hand side of all dynamic equations of the EHB model of Eq. (15). The extra term $\upsilon(t)$ accounts for all model uncertainties including possible parameter variations and nonlinear friction forces in the mechanical and hydraulic parts, as Ref. [4].

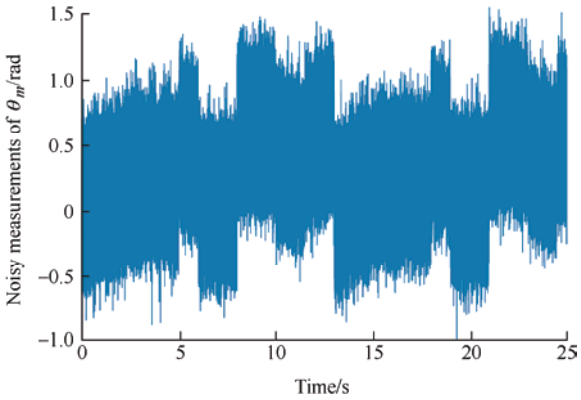

Fig. 7 Noisy measurement of θ_m (Gaussian type)

For all simulations, the reference braking pressure p_{mc_ref} of the EHB was chosen to be variable over a 13 s cycle (and similarly for p_{mc} owing to the control loop by PID). To demonstrate the effectiveness of the observer, the P_{mc} cycle was repeated more than twice during each simulation test. The states of the system and observer are initialized as follows $\omega_{m\text{-}init}=i_{init}=p_{mc\text{-}init}=0$, $\hat{\omega}_{m\text{-}init}=5$, $\hat{i}_{init}=1$, and $\hat{p}_{mc\text{-}init}=10$.

5.2 Measurement noise effect on HGO

To highlight the need for an FHGO, the performance of SHGO in Eq. (31) is presented in this subsection. The simulation scheme is illustrated in Fig. 8. The SHGO gain θ was set to 100 to avoid a slow convergence and high noise amplification.

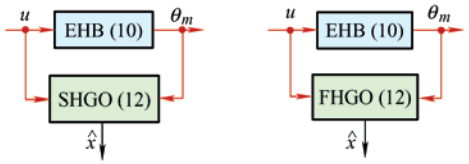

(a) Block diagram for SHGO (b) Block diagram for FHGO

Fig. 8 Block diagrams of the proposed observers for EHB

The master cylinder pressure P_{mc} and its estimates in the absence and presence of measurement noise are illustrated in Fig. 9, which shows the negative effect of noise on the state estimation. Hence, FHGO must be used to compensate for the measurement noise.

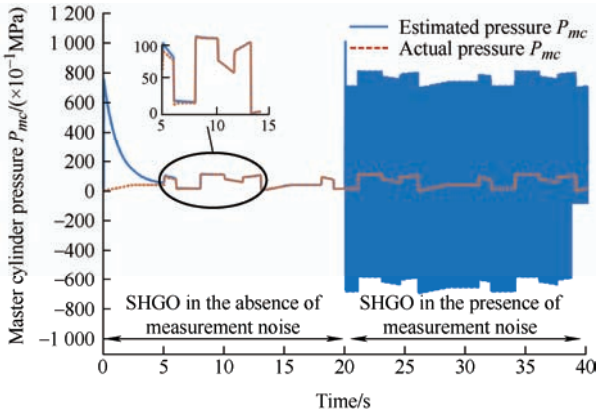

Fig. 9 SHGO performance: Master cylinder pressure p_{mc} estimation in the absence and presence of measurement noise

5.3 Performance of the FHGO with fixed parameters

In this subsection, the FHGO performances with fixed parameters θ and κ are tested under the same simulation protocol. The simulation scheme is shown in Fig. 8b. In order to obtain a fair comparison, the θ parameter has been chosen to be equal to 100 as in the SHGO case. Based on several tests and according to Theorem 1, the appropriate numerical values of κ and r are given by $\kappa = 0.069$ and $r = 3$, respectively.

Fig. 10 shows the master cylinder pressure and its filtered estimation. The impact of measurement noise on the asymptotic behavior of the estimation error was well mitigated. However, Fig. 10 (zoom) shows that the transient period of the FHGO with fixed parameters suffers from a peaking phenomenon.

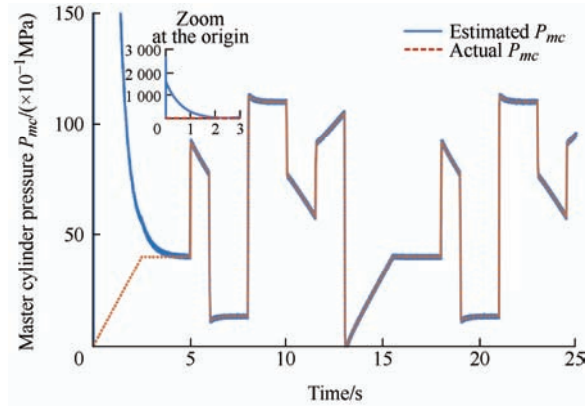

Fig. 10 FHGO performance: Master cylinder pressure P_{mc} estimation

5.4 Performances of FHGO with ES optimization

The superior performances of the proposed FHGO in Eq. (47) for the EHB model in Eq. (29) with the ES optimization of θ and κ are shown in this subsection. The measurement noise is considered to be a sinusoidal signal. A simulation test was also performed using the same protocol. The simulation scheme is shown in Fig. 5. The parameters k_P, k_i, and k_d of the PID-like controller used in the simulation were chosen using the Ziegler-Nichols method. The obtained values are 0.45, 2.33, and 7×10^{-2}.

The parameters of the Newton-based extremum-seeking loop shown in Fig. 5 are listed in Tab. 2. The initial condition of the Hessian inverse $\boldsymbol{\Gamma}(0)$ is chosen to be symmetric and negative definite as [14]

$$\boldsymbol{\Gamma}(0) = \begin{bmatrix} -1 & 2 \\ 2 & -6 \end{bmatrix}$$

Tab. 2 Newton extremum seeking parameters values

Parameter	Value	Parameter	Value
ω	0.1	a	0.1
δ	0.1	$(\breve{\omega}_1, \breve{\omega}_2)$	(7 000, 6 000)
$\breve{\omega}_r$	1	$(\breve{d}_1, \breve{d}_2)$	(350, 610)

The performances of the optimized FHGO are illustrated in Figs. 11 and 12. Fig. 11a shows that the noisy measurable state θ_m is well-filtrated and estimated by the FHGO, which is similar to that for the motor speed ω_m and motor current i, as depicted by Figs. 11b and 11c. The simulated master cylinder pressure p_{mc} and its estimate are shown in Fig. 11d. It can be observed that p_{mc} is well estimated and filtered, and unlike FHGO with fixed parameters (Fig. 10), the FHGO with ES optimization is a peaking-free observer. The optimized gain θ is given in Fig. 12.

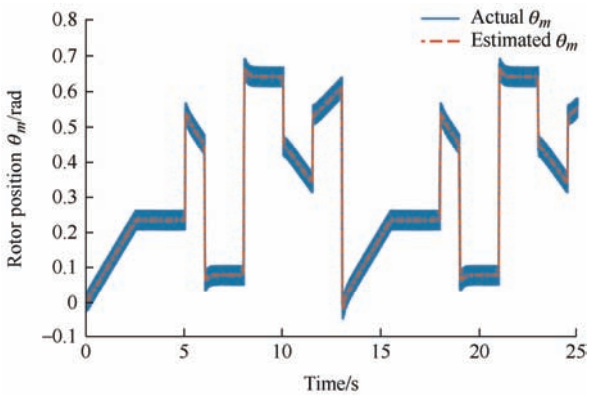

(a) Noisy measurable state θ_m and its estimate

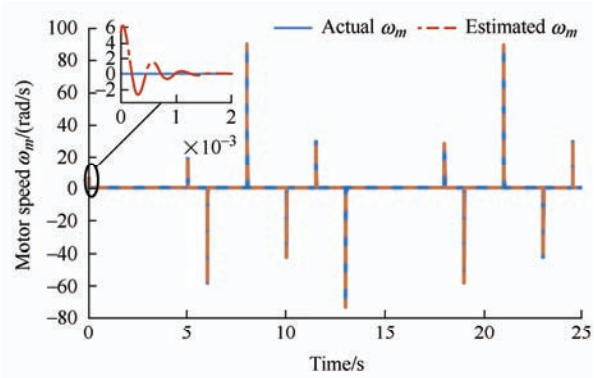

(b) Motor speed ω_m and its estimate

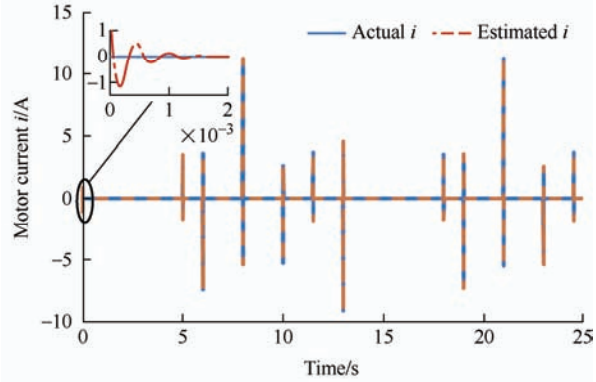

(c) Motor current i and its estimate

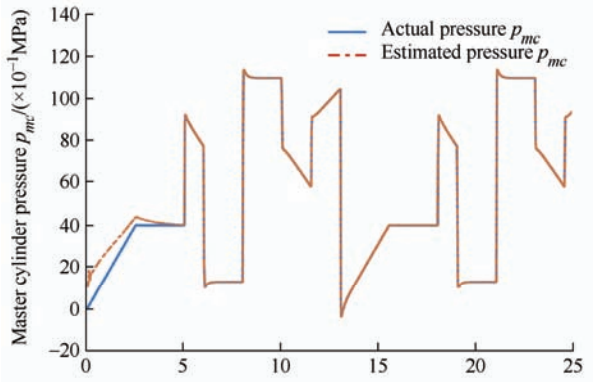

(d) Master cylinder pressure p_{mc} and its estimate

Fig. 11 Performance of FHGO with ES optimization

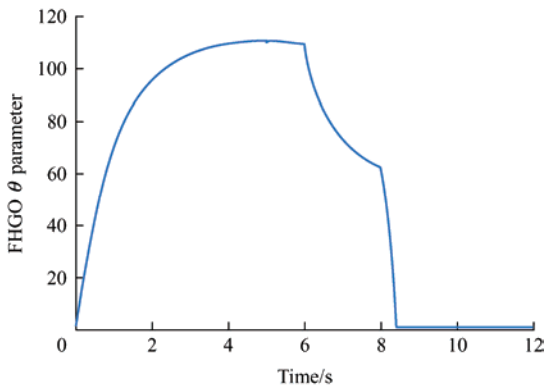

Fig. 12 FHGO θ parameter optimization

5.5 Performance of the optimized FHGO in presence of Gaussian measurement noise

In this subsection, Gaussian noise with a variance of 0.000 5 is considered to demonstrate the capability of the proposed FHGO to achieve a good estimation performance despite varying measurement noises. A simulation test was also performed using the same protocol. The noisy measurement state of θ_m is shown in Fig. 7.

The estimation error behavior of the optimized FHGO in the presence of Gaussian noise is shown in Fig. 13. These figures show that the states θ_m and p_{mc} are well estimated (without the peaking phenomenon), and their estimates are well filtered by the FHGO observer.

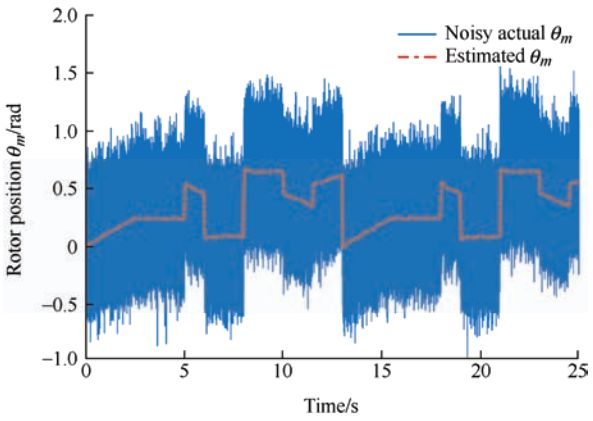

(a) Noisy measurable state θ_m and its estimate

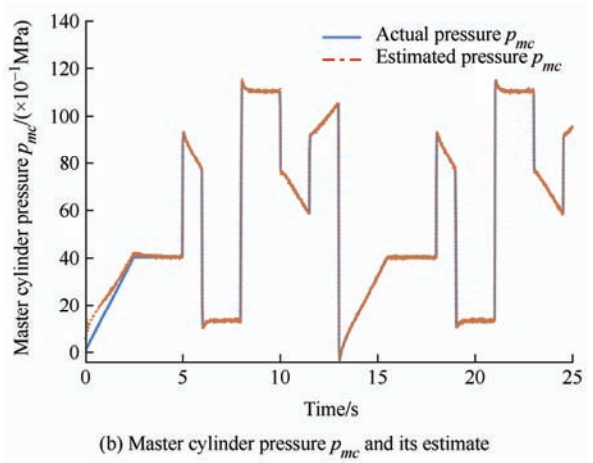

(b) Master cylinder pressure p_{mc} and its estimate

Fig. 13 Performance of the optimized FHGO in the presence of Gaussian measurement noise

5.6 Results and discussion

For a clear comparison, the performances of the proposed observers are summarized in Tab. 3. For the two types of noise signals used in the simulation, the

infinity norm of the master cylinder pressure estimation error $\| \tilde{p}_{mc} \|_\infty$ and the initial peak value of the estimated master cylinder pressure $\hat{p}_{mc}(0)$ (starting from $\hat{p}_{mc\text{-}init} = 10$ bar(1 bar=0.1 MPa)) are shown in Tab. 3. Note that $\| \tilde{p}_{mc} \|_\infty$ and $\hat{p}_{mc}(0)$ are indicated by bars.

Tab. 3 Performance comparison of the proposed observers in the presence of two types of measurement noise

Noise type	SHGO	FHGO with fixed parameters		Optimized FHGO	
	$\| \tilde{p}_{mc} \|_\infty$	$\| \tilde{p}_{mc} \|_\infty$	$\hat{p}_{mc}(0)$	$\| \tilde{p}_{mc} \|_\infty$	$\hat{p}_{mc}(0)$
Sinusoidal	705.3	1.32	2 622	0.227	8.6
Gaussian	737.6	2.27	2 657	1.07	8.86

The simulation graphs are shown in Figs. 9-13 and the performance indices are reported in Tab. 3. The following conclusions were drawn.

(1) The asymptotic behavior of the SHGO in the presence of measurement noise is not guaranteed. Therefore, the structure is not recommended for practical applications.

(2) FHGO with fixed parameters can guarantee good state estimation and noise suppression, but clearly suffers from the peak phenomenon.

(3) The FHGO with ES optimization can achieve a good estimation performance for both types of measurement noise. It exhibits excellent asymptotic behavior with a relatively negligible estimation error and a low peak value at the origin.

Based on the above points, the proposed FHGO with ES-based parameter optimization provides a good estimation of the EHB states, regardless of the type of measurement noise. In addition, it can qualify as a peak-free observer. The optimization of FHGO is highly recommended for practical EHB.

6 Conclusions and perspectives

The issue of online estimation of rotor position, rotor speed, motor current, and master cylinder pressure of an EHB for EVs in the presence of noise was addressed in this study. A filtered high-gain observer (FHGO) was proposed for EHBs. First, an EHB state-space model with four state variables is described. The EHB observability was then checked, and a model transformation by diffeomorphism to a uniformly observable form was carried out. The FHGO for the estimation of EHB model state variables was designed, and observer stability analysis using the Lyapunov theory was proved. To avoid the complexity of the FHGO setting parameters and achieve better FHGO performance, an online ES optimization of the observer tuning parameters was performed. The theoretical results were validated by simulations using the Matlab/Simulink software. The results demonstrated the high performance and robustness of the proposed FHGO. The experimental validation of the observer offered for the EHB system is considered as the perspective of this study. We also plan to perform ES-based optimization to optimally select the *r* order of the low-pass filter.

References

[1] F Ji, Y Pan, Y Zhou, et al. Energy recovery based on pedal situation for regenerative braking system of electric vehicle. *Vehicle System Dynamics*, 2020, 58(1): 144-173.

[2] J El-Bakkouri, H Ouadi, A Saad. Adaptive neuro fuzzy inference system based controller for electric vehicle's hybrid ABS braking. *IFAC-PapersOnLine*, 2022, 55(12): 371-376.

[3] Z Yu, S Xu, L Xiong, et al. An integrated electro-hydraulic brake system for active safety. *SAE Technical Papers*, 2016: 2016-01-1640.

[4] L Xiong, W Han, Z Yu. Adaptive sliding mode pressure control for an electro-hydraulic brake system via desired-state and integral-antiwindup compensation. *Mechatronics*, 2020, 68: 102359.

[5] F Todeschini, M Corno, G Panzani, et al. Adaptive cascade control of a brake-by-wire actuator for sport motorcycles. *IEEE/ASME Transactions on Mechatronics*, 2015, 20(3): 1310-1319.

[6] A Dardanelli, G Alli, S M Savaresi. Modeling and control of an electro-mechanical brake-by-wire actuator for a sport motorbike. *IFAC Proceedings Volumes*, 2010, 43(18): 524-531.

[7] R De Castro, F Todeschini, R E Araújo, et al. Adaptive-robust friction compensation in a hybrid brake-by-wire actuator. *Proceedings of the Institution of Mechanical Engineers*, *Part I*: *Journal of Systems and Control Engineering*, 2014, 228(10): 769-786.

[8] W Han, L Xiong, Z Yu. Braking pressure tracking control of a pressure sensor unequipped electro-hydraulic booster

based on a nonlinear observer. *SAE Technical Papers*, 2018: 1-7.

[9] M Shakarami, K Esfandiari, A A Suratgar, et al. Peaking attenuation of high-gain observers using adaptive techniques: State estimation and feedback control. *IEEE Transactions on Automatic Control*, 2020, 65(10): 4215-4229.

[10] A Barra, H Ouadi, F Giri, et al. Sensorless nonlinear control of wind energy systems with doubly fed induction generator. *Journal of Control*, *Automation and Electrical Systems*, 2016, 27(5): 562-578.

[11] A A Prasov, H K Khalil. A nonlinear high-gain observer for systems with measurement noise in a feedback control framework. *IEEE Transactions on Automatic Control*, 2013, 58(3): 569-580.

[12] D Astolfi, L Zaccarian, M Jungers. On the use of low-pass filters in high-gain observers. *Systems & Control Letters*, 2021, 148: 104856.

[13] M Farza, A Ragoubi, S Hadj Saïd, et al. Improved high gain observer design for a class of disturbed nonlinear systems. *Nonlinear Dynamics*, 2021, 106(1): 631-655.

[14] A Ghaffari, M Krstić, D Nešić. Multivariable Newton-based extremum seeking. *Automatica*, 2012, 48(8): 1759-1767.

[15] Y Zhou, Z Wang, J Wang. Illumination-resilient lane detection by threshold self-adjustment using Newton-based extremum seeking. *IEEE Transactions on Intelligent Transportation Systems*, 2022, 23(10): 18643-18654.

[16] S Gheouany, H Ouadi, F Giri, et al. Experimental validation of multi-stage optimal energy management for a smart microgrid system under forecasting uncertainties. *Energy Conversion and Management*, 2023, 291: 117309.

[17] W Han, L Xiong, Z Yu. A novel pressure control strategy of an electro-hydraulic brake system via fusion of control signals. *Proceedings of the Institution of Mechanical Engineers*, *Part D*: *Journal of Automobile Engineering*, 2019, 33(13): 3342-3357.

[18] J P Gauthier, I Kupka. Deterministic observation theory and applications. Cambridge: Cambridge University Press, 2001.

[19] H K Khalil. Nonlinear systems. New York: Pearson Education Limited, 2014.

[20] D Astolfi, L Marconi, L Praly, et al. Low-power peaking-free high-gain observers. *Automatica*, 2018, 98: 169-179.

Jamal El-bakkouri received his M.S. degree in Electrical Engineering from ENSAM, Mohammed V University of Rabat, Morocco, in 2019. He obtained a Ph.D. degree in Electrical Engineering and Automatic Control from the National High School for Electricity and Mechanics of Casablanca, Morocco, in 2023. Since 2009, he has been an Aggregate (agrégé) Professor of Electrical Engineering in preparatory classes for engineering schools.

His research interests include the nonlinear optimization, observation, and control of dynamic systems, in particular, regenerative and electro-hydraulic braking systems for electric vehicles. He currently serves as a reviewer at the IFAC World Congress 2023.

Hamid Ouadi received his degree as Associate Professor of Electrical Engineering from the ENS of Cachan, France, in 1995. He received his Ph.D. in Science from the Mohammedia School of Engineers of Rabat, Morocco, in 2004, and his doctoral research subject was the observation and control of asynchronous machines. He is currently a Full Professor at Mohammed V University of Rabat. He has published 1 book, 28 journal papers, and 47 conference papers.

His research activities are focused on the control of nonlinear systems, such as the observation and control of renewable energy systems and braking/traction systems of electric vehicles. He is also active in smart-grid energy management and power electronic systems.

Fouad Giri received a Ph.D. in Automatic Control from the National Polytechnic Institute of Grenoble, France, in 1988. He is currently a Professor at the University of Caen-Normandy, France. His research interests include nonlinear system identification, observation, and control for finite- and infinite-dimensional systems and their application to electric power systems. He has authored six books and more than 120 journal papers. He has served as Chair of the IFAC TC1.2 and Associate Editor for several journals, including Automatica, Control Engineering Practice, and IEEE Transactions on Control Systems Technology.

Mohamed Khafallah received B.Sc., M.Sc., and Ph.D. degrees in Electrical Engineering from Hassan II University, Casablanca, in 1989, 1991, and 1995, respectively. In 1995, he joined the National High School of Electricity and Mechanics (ENSEM), Hassan II University, Casablanca, Morocco, where he is currently a Professor in the Department of Electrical Engineering and Chief of Laboratory Energy and Electrical Systems (LESE). His main research interests include applications in power electronic conversion and motor drives. He has published numerous research papers and book chapters in international journals and conference proceedings.